Portland State University

PDXScholar

3-1-2021

Inferring the Subsurface Geometry and Strength of Slow-Moving Landslides Using 3-D Velocity Measurements from the NASA/JPL UAVSAR

Alexander L. Handwerger
University of California, Los Angeles

Adam M. Booth
Portland State University, boothad@pdx.edu

Mong-Han Huang
University of Maryland at College Park

Eric J. Fielding
California Institute of Technology

Citation Details

JGR Earth Surface

Key Points:
- Landslide thickness can vary by tens of meters within a single landslide
- The largest landslide complexes get larger by increasing area rather than increasing thickness
- Landslide strength is scale-dependent, such that large landslides tend to be weaker than small landslides

Supporting Information:
- Supporting Information S1
- Table S1
- Table S2

Correspondence to:
A. L. Handwerger,
alexander.handwerger@jpl.nasa.gov

Inferring the Subsurface Geometry and Strength of Slow-Moving Landslides Using 3-D Velocity Measurements From the NASA/JPL UAVSAR

**Alexander L. Handwerger**[1,2] , **Adam M. Booth**[3] , **Mong-Han Huang**[4] , and **Eric J. Fielding**[2]

[1]Joint Institute for Regional Earth System Science and Engineering, University of California, Los Angeles, Los Angeles, CA, USA, [2]Jet Propulsion Laboratory, California Institute of Technology, Pasadena, CA, USA, [3]Department of Geology, Portland State University, Portland, OR, USA, [4]Department of Geology, University of Maryland, College Park, MD, USA

Abstract The hazardous impact and erosive potential of slow-moving landslides depends on landslide properties including velocity, size, and frequency of occurrence. However, constraints on size, in particular, subsurface geometry, are lacking because these types of landslides rarely fully evacuate material to create measurable hillslope scars. Here, we use pixel offset tracking with data from the NASA/ JPL Uninhabited Aerial Vehicle Synthetic Aperture Radar to measure the three-dimensional surface deformation of 134 slow-moving landslides in the northern California Coast Ranges. We apply volume conservation to infer the actively deforming thickness, volume, geometric scaling, and frictional strength of each landslide. These landslides move at average rates between $\sim$0.1–2 m/yr and have active areas of $\sim$6.10 $\times$ 10^3–2.35 $\times$ 10^6 m^2, inferred mean thicknesses of $\sim$1.1–25 m, and volumes of $\sim$7.01 $\times$ 10^3– 9.75 $\times$ 10^6 m^3. The best fit volume-area geometric scaling exponent is $\gamma \sim$ 1.2–1.5, indicating that these landslides fall between typical soil and bedrock landslide scaling. A rollover in the scaling relationship suggests that the largest landslide complexes in our data set become large primarily by increasing in area rather than thickness. In addition, the slow-moving landslides display scale-dependent frictional strength, such that large landslide tend to be weaker than small landslides. This decrease in frictional strength with landslide size is likely because larger landslides are composed of higher proportions of weak material. Our work shows how state of the art remote sensing techniques can be used to better understand landslide processes and quantify their contribution to landscape evolution and hazards to human safety.

1. Introduction

Landslides are a major natural hazard and are often the dominant process that erodes mountainous landscapes (Korup et al., 2007; Larsen et al., 2010; Mackey & Roering, 2011; Simoni et al., 2013). Both their hazardous impact and erosive potential depend on landslide properties including the velocity, size, and frequency of occurrence. Measuring these landslide properties is challenging because landslides exhibit a wide range of velocities (mm/yr to m/s), spatial areas (10^0–10^8 m^2), and volumes (10^{-1}–10^{10} m^3), and can occur in large numbers (hundreds to tens of thousands) over broad spatiotemporal scales (Cruden & Varnes, 1996; Hungr et al., 2014; Lacroix, Handwerger, et al., 2020; Larsen et al., 2010). Importantly, the landslide failure style also impacts our ability to measure landslide properties, such as thickness and volume, which can strongly influence runout and erosion rate (e.g., Korup et al., 2007; Larsen et al., 2010; Legros, 2002). Some landslides create clear and identifiable scars and deposits by evacuating material from the hillslope, making it possible to directly measure landslide properties from field data, digital elevation models (DEMs), and remote sensing observations (e.g., Bessette-Kirton et al., 2018; Warrick et al., 2019; Wartman et al., 2016). However, for landslides that move slowly for years or centuries (Lacroix, Handwerger et al., 2020; Mackey et al., 2009; Rutter & Green, 2011), referred to as slow-moving landslides, and do not create hillslope scars, it is difficult to constrain their thickness and volume because data are usually limited to isolated point measurements from boreholes (Schulz et al., 2018; Simoni et al., 2013; Travelletti & Malet, 2012), which do not capture the spatial variability exhibited by these landslides. It is therefore advantageous to develop and apply tools and methods that can be used to construct large inventories of slow-moving landslides and quantify their surface and subsurface properties.
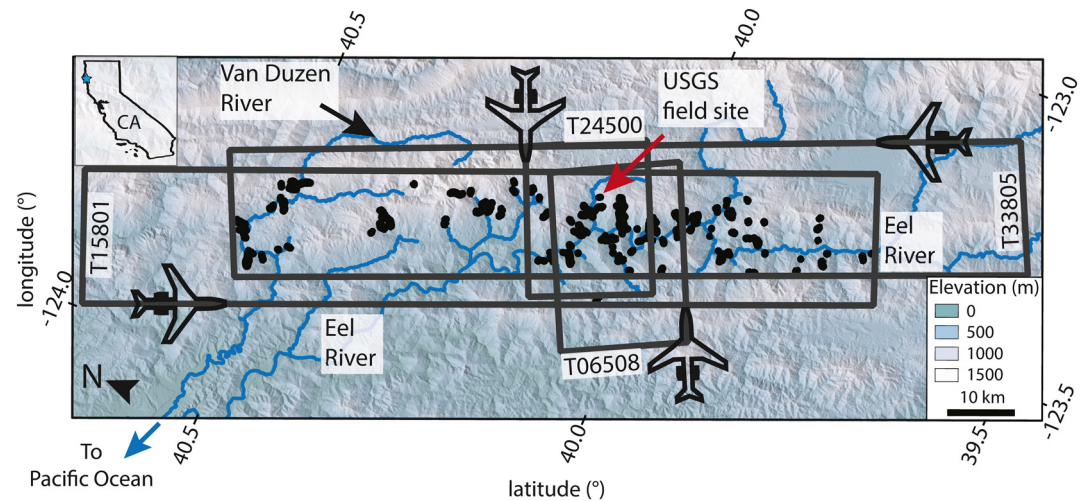
Figure 1. Map of our northern California Coast Ranges study site. Black polygons outline the active landslides analyzed in this study. Elevation (m) shown by green to white color gradient. Black boxes show the left-looking UAVSAR swaths and corresponding track numbers with airplanes showing flight direction. Red arrow shows the location of a U.S. Geological Survey (USGS) landslide field site. Blue lines show major rivers and some tributaries in landslide areas. Inset shows a map of California with a star corresponding to the study site.

Modern remote sensing tools, such as synthetic aperture radar (SAR), optical imagery, and lidar, provide high-resolution measurements of topography and ground surface deformation that can be used to identify and monitor landslides with millimeter- to centimeter-scale accuracy at spatial resolutions of a few centimeters to hundreds of meters. Recent work using pixel offset tracking and SAR interferometry with these data has quantified the two-dimensional (2-D) and three-dimensional (3-D) surface deformation of slow-moving landslides (Aryal et al., 2015; Booth et al., 2020; Hu et al., 2020; Lacroix, Dehecq, et al., 2020; Stumpf et al., 2017; Travelletti et al., 2014). These studies, along with numerous ground-based investigations (e.g., Iverson & Major, 1987; Malet et al., 2002; Schulz et al., 2017), have shown that slow-moving landslides exhibit nonuniform spatial and temporal kinematic patterns. In addition, high-resolution 3-D surface deformation measurements can be used to infer the thickness and subsurface geometry of the actively moving part of the landslide. Previous studies (Aryal et al., 2015; Booth et al., 2020; Booth, Lamb, et al., 2013; Delbridge et al., 2016; Hu et al., 2020) have suggested that the active landslide thickness can vary by tens of meters within a single landslide, and the slip surfaces have an irregular and bumpy morphology that differs considerably from commonly assumed, idealized geometric forms, such as semicircles, ellipsoids, and log spirals (see a detailed review paper by Michel et al., 2020). These large changes in thickness within a single landslide mass have important implications for estimating volume and sediment flux, designing field instrumentation and landslide mitigation strategies, and determining the stresses that control landslide kinematics. Although techniques that invert surface observations for subsurface characteristics are becoming more common, most studies have focused on individual landslides occurring under different and site-specific environmental conditions, making it difficult to identify more generic geometric scaling relations for slow-moving landslides.

In this study, we use data from the NASA/JPL Uninhabited Aerial Vehicle Synthetic Aperture Radar (UAVSAR) to construct an inventory of 134 active slow-moving landslides in a ~ 1,621 km^2 area of the northern California Coast Ranges between 2016 and 2019 (Figure 1). These landslides occur in the Eel River catchment, a region well-known for its slow-moving landslides, and are driven by high seasonal rainfall (Bennett et al., 2016; Booth, Roering, et al., 2013; Handwerger et al., 2013, 2015, 2019; Handwerger, Huang, et al., 2019; Kelsey, 1978; Mackey & Roering, 2011; Mackey et al., 2009; Roering et al., 2009, 2015; Schulz et al., 2018). The landslides are underlain by the Central Belt Franciscan mélange, a mechanically weak and pervasively sheared bedrock with an argillaceous matrix that surrounds blocks of stronger rock types, including sandstone, chert, and greenstone (Jayko et al., 1989; Jennings et al., 1977; McLaughlin et al., 1982, 2000). We measure the 3-D surface deformation and geometry of each landslide, and use these data in a volume conservation framework to invert for their active thickness, volume, and strength. We derive new

geometric scaling relations for slow-moving landslides and make comparisons with a worldwide inventory of soil and bedrock landslides. Our work is the first to use volume conservation methods to invert for the thickness of a large inventory of landslides, and this approach could be applied to other groups of slow-moving landslides around the world. Our work also shows how state of the art remote sensing techniques can be used to better understand landslide processes and quantify their contribution to landscape evolution.

2. Materials and Methods

2.1. UAVSAR Data and Processing

We use SAR data acquired by the NASA/JPL UAVSAR airborne system for our landslide investigation. UAVSAR has a left-looking radar attached to a NASA Gulfstream III airplane that operates with a L-band wavelength (~23.8 cm) and a swath width of ~20 km. The NASA Gulfstream III autopilot flies at 13 km above sea level and repeats the flight lines within a 5 m radius tube, so the spatial baselines are always short and have no impact on deformation measurements. UAVSAR data have a pixel spacing of 1.67 m in the range direction (measured along the line-of-sight) and 0.6 m in the azimuth direction (measured along the UAVSAR flight direction). We designed the UAVSAR data collection for the northern California Coast Ranges site specifically to monitor a large quantity of slow-moving landslides that were initially identified by several previous studies (e.g., Bennett, Miller, Roering, & Schmidt, 2016; Handwerger et al., 2015; Kelsey, 1978; Mackey & Roering, 2011; Roering et al., 2009). Some of these UAVSAR data were used in a recent study by Handwerger et al. (2019) to analyze changes in landslide activity due to extreme rainfall. We collected data on four partially overlapping flight paths to increase data redundancy and to provide between 4 and 8 independent deformation measurements (Figure 1). There were 12 data acquisitions at our field site between April 2016 and May 2019. The time between data acquisitions ranges between 47 and 237 days, with a mean of 104 days (Table S1). UAVSAR Single-Look Complex (SLC) data are freely available at https://uavsar.jpl.nasa.gov/.

We perform pixel offset tracking on the coregistered UAVSAR stack SLC data using the *Ampcor* module, which is part of the JPL InSAR Scientific Computing Environment (ISCE) version 2 software package (Rosen et al., 2012). Pixel offset tracking (sometimes referred to as subpixel correlation) uses cross-correlation between SAR amplitude images to quantify image offsets (i.e., displacement) due to ground surface motion in two dimensions; 1) the range or look direction, and 2) the azimuth or along-track direction (e.g., Fialko et al., 2001; Fielding et al., 2020; Pathier et al., 2006). We use the terms range/look direction and azimuth/along-track direction, interchangeably. Pixel tracking has a precision up to ~1/10 of the pixel size, which corresponds to ~6 cm in the along-track direction and ~17 cm in the range direction for a pair of UAVSAR images. Although this technique is less precise than conventional InSAR, it does not involve phase unwrapping and thus is better suited for measuring the decimeter- to meter-scale displacements commonly displayed by many slow-moving landslides (Lacroix, Handwerger, et al., 2020). To account for the differences in the range and along-track pixel size, we use a cross-correlation window length of 128 pixels with a skip size of 32 pixels (distance between matching window calculations) in the along-track direction and a cross-correlation window width of 64 pixels with a skip size of 16 pixels in the range direction, resulting in a window size of 77 m by 107 m. This cross-correlation window size was found to provide the best landslide deformation signal from UAVSAR pixel offset tracking by Handwerger et al. (2019). We geocode the pixel offset measurements to a 0.4 arcsecond (~12 m) pixel using the TanDEM-X DEM provided by the German Aerospace Center (DLR). We process all possible combinations of pixel offset tracking pairs, which results in 66 pixel offset tracking maps on each track (264 in total) with single pair time spans ranging from 47 to 1,148 days (Table S1). We exclude 35 poor-quality pixel offset tracking maps from our analysis that included a large number of pixels with physically incorrect displacements (e.g., upslope motion or unusually large values) and significant noise that obscured the landslide signals. We found these poor-quality data tend to result from long duration pairs that exceed ~2 years, which are subject to numerous changes in the ground surface (e.g., vegetation changes, anthropogenic changes) that can deteriorate the cross-correlation result (Table S1). We convert all of the displacement offset maps to velocities and then take the temporal average of the 31 remaining pixel offset velocity maps to make a mean velocity map for our thickness inversions.

2.2. Three-Dimensional Ground Surface Deformation

To solve for 3-D deformation from SAR requires at least three independent measurements of surface deformation. Each UAVSAR flight path provides two independent measurements of surface motion from pixel offset tracking (i.e., along-track and range). Therefore, using pixel offset tracking velocity maps, data from at least two flights is required for 3-D inversions. Because UAVSAR acquires data on four different flight paths in our field area (Figure 1), we have a maximum of eight deformation measurements in the central region of our field area where all four flight paths overlap and a maximum of four deformation measurements in the northern and southern extents where only two flight paths overlap. Thus, we are always able to achieve an overdetermined 3-D inversion.

Each deformation measurement from pixel tracking is composed of the true displacement vector projected onto the along-track or range direction of the UAVSAR. We use a least squares inversion to isolate the east, north, and vertical components of deformation defined in the form $\mathbf{d} = \mathbf{Gm}$,

$$
\begin{bmatrix} v_{\text{rng1}} \\ v_{\text{azi1}} \\ \vdots \\ v_{\text{rng},M} \\ v_{\text{azi},M} \end{bmatrix} = \begin{bmatrix} \cos\xi 1 \sin\theta_1 & \sin\xi_1 \sin\theta_1 & -\cos\theta_1 \\ \cos\xi_1 & \sin\xi_1 & 0 \\ \vdots & \vdots & \vdots \\ \cos\xi_M \sin\theta_M & \sin\xi_M \sin\theta_M & -\cos\theta_M \\ \cos\xi_M & \sin\xi_M & 0 \end{bmatrix} \begin{bmatrix} v_{\text{ew}} \\ v_{\text{ns}} \\ v_{\text{ud}} \end{bmatrix},
\tag{1}
$$

where $v_{\text{rng},M}$ is the range (or look direction) velocity, $v_{\text{azi},M}$ is the azimuth (or along-track direction) velocity, M is the flight path number (minimum of two needed for pixel offset tracking), ξ is the UAVSAR heading direction (i.e., along-track direction) with counterclockwise as positive, θ is the UAVSAR look angle, and v_{ew}, v_{ns}, v_{ud} are the east-west, north-south, and vertical components of velocity, respectively.

The overdetermination of the 3-D inversion allows us to constrain the uncertainty from the inversion (e.g., Delbridge et al., 2016). To constrain the inversion uncertainty, we repeat the 3-D inversion multiple times using different combinations of v_{rng} and v_{azi}. For instance, for landslides with eight deformation measurements (i.e., four range and four azimuth measurements), we perform the 3-D inversion 198 times using between three and eight deformation measurements. We then take the mean and standard deviation of all of the inversions and use these values as the 3-D velocities and inversion uncertainty, respectively. We further constrain the uncertainty in our velocity measurements by examining the apparent deformation rate of stable hillslopes. To reduce noise and error (i.e., unrealistically large displacements), we apply velocity thresholds and mask out pixels with apparent velocities > 50 m/yr, which is much faster than the typical velocity range displayed by the northern California Coast Ranges landslides (Bennett et al., 2016; Handwerger et al., 2019; Roering et al., 2015). We also mask out pixels that have mean velocities less than their inversion uncertainty and use nearest neighbor interpolation with a five-pixel maximum radius to fill in these masked pixels.

2.3. Landslide Thickness Inversion

We use 3-D surface velocity measurements from pixel offset tracking to infer the thickness, volume, and shear zone geometry of the active parts of each landslide using a conservation of volume approach. We apply the method originally described by Booth, Lamb, et al. (2013) and more recently by Booth et al. (2020), which assumes that during our ~3-year study period, the measured surface velocity is representative of the depth-averaged velocity, the sliding surface does not change in time, there is minimal direct erosion or deposition of the landslide surface, and the landslide material density is uniform and constant. While landslides may violate these assumptions in general, they are reasonable for our study area for the following reasons: (1) at the Two Towers landslide, a USGS instrumented landslide in our study site (Schulz et al., 2018), the measured surface velocity was approximately equal to the depth-averaged velocity, and a narrow shear zone was identified (Figure S1); (2) the landslides were continuously active with fixed spatial boundaries over the time periods that 3-D displacements were measured, suggesting movement on the same slip surface; (3) minor amounts of direct surface erosion or deposition were likely confined to gully systems on the landslides' surfaces, which occupy a small percentage of the landslides' surface area (~1%) and therefore

have a minimal effect on the inversion; and (4) dilation/compaction or shrinking/swelling that would cause changes in density is likely on the order of centimeters or less (Booth et al., 2020; Delbridge et al., 2016; Iverson, 2005; Schulz et al., 2018), which is typically small compared to surface velocity gradients, thus having limited influence of the measured 3-D surface velocity. Therefore, for a landslide of constant density with no erosion or deposition, conservation of volume implies that

$$v_{\mathrm{ud}} = \nabla \cdot \left(\overline{u} h \right) + u_{\mathrm{surf}} \cdot \nabla z_{\mathrm{surf}}, \tag{2}$$

where v_{ud} is the vertical component of the 3-D landslide surface velocity vector, h is the active landslide thickness, u_{surf} is the vector of horizontal components of landslide surface velocity, $\overline{u}$ is the depth-averaged vector of horizontal components of landslide velocity, and z_{surf} is the surface elevation measured from the $\sim$12 m TanDEM-X DEM. The first term on the right-hand side of Equation 2 is the contribution of flux divergence to the vertical component of the surface velocity, and the second term is the contribution due to advection of the sloped land surface. Because UAVSAR measures the velocity of the ground surface, u_{surf}, we assume that $\overline{u} = f u_{\mathrm{surf}}$, where f is a constant that characterizes the thickness of the shear zone at the base of the landslide relative to the total landslide thickness. We constrain f using borehole inclinometer data from two boreholes at the USGS field station on the Two Towers landslide (supporting information and Figure S1). Unfortunately, the Two Towers landslide is not detectable with pixel tracking from UAVSAR data because the landslide is small (250 m long and 40 m wide) and moving too slowly (maximum speed $\sim$6 cm/yr) (Schulz et al., 2018). Using these data, we find that $f \sim 0.96$, which indicates that the landslide moves along a narrow shear zone with the material above translating essentially as a rigid block. For simplicity, we assume that $f = 1$ and that the landslides move as a rigid block. Other studies in California (e.g., Keefer & Johnson, 1983; Swanston et al., 1995) and around the world (e.g., Simoni et al., 2013; van Asch & van Genuchten, 1990) have also found that similar type slow-moving landslides move as a rigid plug above a narrow shear zone such that $f \sim 1$ is a reasonable approximation, however more ground-based investigations are required to better constrain the f parameter for multiple landslides. Although f generically represents the ratio of depth-averaged to surface velocity, it can be related to specific rheologies if desired (Booth, Lamb, et al., 2013; Delbridge et al., 2016) and we discuss the implications of different f values in Section 4.2.

Incorporating f into Equation 2 gives

$$v_{\mathrm{ud}} = \nabla \cdot \left(f u_{\mathrm{surf}} h \right) + u_{\mathrm{surf}} \cdot \nabla z_{\mathrm{surf}}, \tag{3}$$

which is a statement of conservation of volume in a Lagrangian reference frame (Booth et al., 2020; Delbridge et al., 2016). We discretize Equation 3 using centered finite differences, rearrange it as a system of linear equations, and then solve for thickness by minimizing the value of

$$\left| X h - b \right|^2 + \alpha^2 \left| \nabla^2 h \right|^2, \tag{4}$$

subject to nonnegative constraints, where X is a diagonally dominant matrix that contains the depth-averaged horizontal velocity data, b is a vector defined as $u_{\mathrm{surf}} \cdot \nabla z_{\mathrm{surf}} - v_{\mathrm{ud}}$, and α is a damping parameter to regularize the ill-posed inverse problem. Since both the matrix X and the vector b contain data with uncertainties, and the damping parameter necessarily introduces bias, estimating total uncertainty of the resulting thickness model is not straightforward. However, we make a minimum estimate following standard techniques from inverse theory, which reflects uncertainty in b only (supporting information). We explore a wide range of α from 10^{-3} to 10^{1} and determine the best level of regularization using the Generalized Cross-Validation method (supporting information and Figure S2). We resample our $\sim$12 m pixel spacing grid to square 10×10 m pixel and perform the thickness inversion in the MATLAB software package using the CVX program, a package for specifying and solving convex programs (Grant & Boyd, 2014). For the largest landslide in our inventory (i.e., Boulder Creek landslide complex) we had to downsample the grid to a 20×20 m pixel due to computational limitations. The inferred thickness values represent the best solution that does not violate conservation of volume and assumes that the surface velocity is equal to the depth-averaged velocity.

It is important to further emphasize that the thickness inversions are only relevant to the active parts of landslides such that there needs to be detectable surface deformation to invert for the landslide thickness.

Specifically, the values of *b* (Equation 4) need to differ from background values on known stable ground to infer nonzero thicknesses. Landslides or areas and kinematic zones within landslides that are not moving are therefore considered to have zero depth. Landslide thickness in this study therefore specifically means the "active thickness" during our study period.

2.4. Landslide Inventory and Geometric Scaling

To select landslides for 3-D surface velocity and thickness inversions, we assemble a new inventory of active landslides in our ~1,621 km^2 study area in the northern California Coast Ranges that includes only those landslides that show a significant deformation signal using the pixel offset tracking method. This limits our analysis to the faster-moving landslides that exhibit rates of decimeters to meters per year. Our landslide inventory was guided by a number of preexisting landslide inventories for the northern California Coast Ranges (Bennett, Miller, Roering, & Schmidt, 2016; Handwerger et al., 2019; Kelsey, 1978; Mackey & Roering, 2011). We map the landslide boundaries in QGIS using the 3-D velocity maps, hillshade maps constructed from 1 m pixel spacing lidar provided by OpenTopography (Roering, 2012), the ~12 m pixel spacing TanDEM-X DEM, and Google Earth imagery. Because slow-moving landslides display nonuniform spatial kinematic zones and complex kinematic histories (e.g., Nereson & Finnegan, 2019; Schulz et al., 2017; Stumpf et al., 2017), there are often differences between the landslide boundaries mapped with kinematic data and those mapped based on geomorphic interpretation of hillshades or aerial photos. These differences in mapping are especially important for our thickness inversions because including the parts of landslides that are not currently moving can cause the thickness inversion to produce unreliable results. Therefore, we use the temporally averaged landslide velocity and only map areas of each landslide that are moving during our study period. For larger landslides with multiple kinematic zones, we perform separate thickness inversions for any isolated, faster-moving areas of the landslide, as well as for the entire landslide complex as a whole. If results had substantially different spatial patterns of thickness, we adopt the more reliable results for the smaller isolated landslides. We use QGIS to quantify the spatial metrics of each landslide, including length, average width (defined as area divided by length), area, and slope angle. We also report the mean, median, 75th percentile, and maximum horizontal velocity, 3-D velocity magnitude, and 3-D inversion velocity errors for each landslide.

We then derive empirical geometric scaling relations for landslide thickness (*h*) and volume (*V*) from the measured landslide area (*A*). Geometric scaling relations are commonly used to quantify erosion rates of large inventories of landslides and are important for understanding landslide mechanics (e.g., Bunn et al., 2020a; Guzzetti et al., 2009; Larsen et al., 2010; Milledge et al., 2014). Larsen et al. (2010) showed that these scaling relations hold over 9 orders of magnitude in area and 12 orders of magnitude in volume. Landslide scaling relations take the form of a power function where

$$V = c_V A^\gamma \text{ and } h = c_h A^\zeta, \tag{5a and 5b}$$

where γ and ζ are scaling exponents and c_V and c_h are the intercepts. We constrain the coefficients of these power functions by log-transforming our data and finding the best fit parameters with 95% confidence intervals using a linear least square inversion in MATLAB.

2.5. Frictional Strength

We estimate the frictional strength of each landslide by following the 3-D Simplified Janbu method (Bunn et al., 2020b; Hungr, 1987; Hungr et al., 1989; Leshchinsky, 2019). This method assumes that the vertical intercolumn shear forces are negligible. Each landslide is discretized into 3-D columns with a surface area S_{basal} and total weight *W*. The basal surface area is defined by

$$S_{\text{basal}} = \Delta x \Delta y \frac{\left(1 - \sin^2 \beta_y \sin^2 \beta_x\right)^{1/2}}{\cos \beta_y \cos \beta_x}, \tag{6}$$

where Δx and Δy are the grid spacing in the x and y direction, respectively, β_x is the local dip angle perpendicular to the direction of motion and β_y is the local dip in the direction of motion. The normal force N at the base of each column is defined by

$$N = \frac{W - CS_{\text{basal}} \sin \beta_x \, / \, F + pS_{\text{basal}} \tan \phi \sin \beta_x \, / \, F}{\cos \Delta_z \left(1 + \dfrac{\sin \beta_x \tan \phi}{F \cos \Delta_z} \right)},$$ (7)

where p is the mean pore pressure acting at the base of each column, C is the cohesion, ϕ is the residual friction angle, F is the factor of safety, and Δ_z is the local dip angle defined in terms of the motion-parallel and motion-perpendicular dips by

$$\cos \Delta_z = \left(\sqrt{\frac{1}{1 + \tan^2 \beta_y + + \tan^2 \beta_x}} \right).$$ (8)

Finally, F is defined by

$$F = \frac{\sum CS_{\text{basal}} \cos \beta_x + \left(N - pS_{\text{basal}} \right) \tan \phi \cos \beta_x}{\sum N \cos \Delta_z \tan \beta_x},$$ (9)

where the summation is over all columns. The numerator is the resisting force, with the term in the parentheses defining the effective normal force, and $\tan\phi$ is the friction coefficient, and the denominator is the shear force. We assume that cohesion is negligible since these landslides are moving, some of which have been moving for decades (Mackey & Roering, 2011). We set $F = 1$ (i.e., balanced forces at failure) and solve for friction angle under both dry and fully saturated (hydrostatic conditions) end members to produce a minimum and maximum estimate. Table S2 shows the dry and wet landslide density values used for our calculations. Recent work by Bunn et al. (2020b) used a similar approach to infer the strength of several hundred landslides in Oregon, USA.

3. Results

3.1. Landslide Inventory and 3-D Velocity

We identified 134 active landslides in our northern California Coast Ranges field site (Figure 1), 19 of which were unmapped by previous studies (Bennett, Miller, Roering, & Schmidt, 2016; Handwerger et al., 2019; Mackey & Roering, 2011). These landslides have average widths from 66 to 556 m, lengths from 68 to 4,727 m, areas from 7.8×10^3 to 2.63×10^6 m^2, and mean slope angles from 10° to 29° (Table S3). Each landslide exhibited a nonuniform spatial velocity pattern (see examples in Figure 2). The spatial kinematic patterns remain fixed during our study period and are similar to those mapped in previous studies (see Bennett et al., 2016; Handwerger et al., 2019; Mackey & Roering, 2011). The maximum 3-D velocity magnitude of the individual landslides, calculated as $v_{\text{3-D}} = (v_{\text{ns}}^2 + v_{\text{ew}}^2 + v_{\text{ud}}^2)^{1/2}$, ranged from 0.198 to 8.58 m/yr. The average 3-D velocity magnitude of the individual landslides ranged from 0.123 to 2.11 m/yr. The landslide motion was always primarily in the downslope direction (see example in Figures 2e and 2f), but at different locations we do measure areas of both uplift and subsidence within a single landslide (see example in Figure 2d). We note that local surface uplift occurs when the vertical component of the velocity vector dips less steeply than the topographic surface at a given point. As a result, the vertical velocity is often still negative even in areas where the topographic surface is locally being uplifted, and only when the vertical motion is upwards relative to horizontal do we observe positive vertical velocities. The mean 3-D velocity uncertainty from the 3-D inversion (Equation 1) for the individual landslides ranged from 0.0179 to 1.91 m/yr. We report the full uncertainty statistics for each individual landslide in Table S3. The 3-D velocity magnitude uncertainty from examining the apparent velocity of stable hillslopes was ≤ 0.1 m/yr.

We classified the slow-moving landslides into three subgroups based on their geometry and kinematic patterns (Table S3). Figure 2 shows three example landslides which we define as slumps, earthflows, and
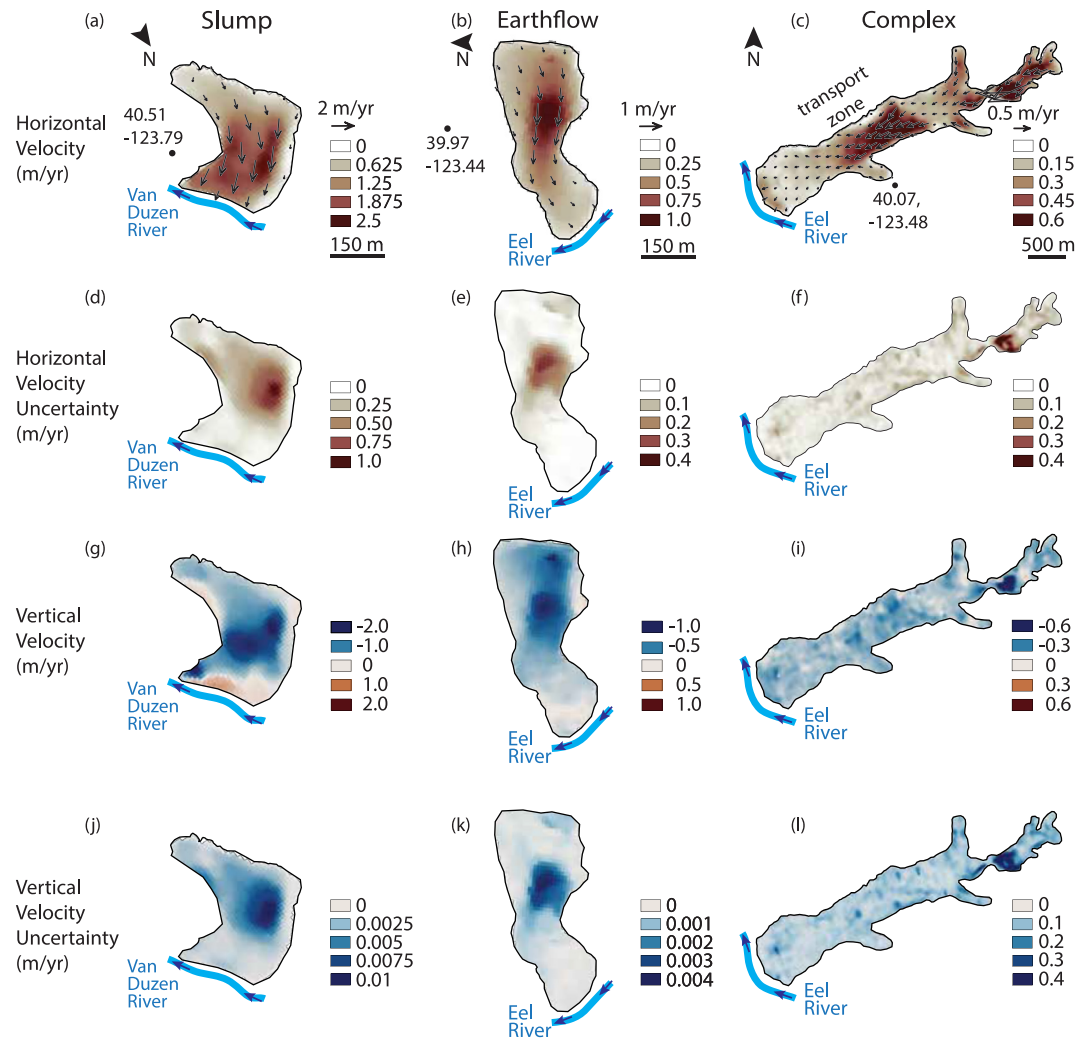
Figure 2. 3-D velocity maps, for example, slump, earthflow, and landslide complex. (a–c) Horizontal velocity maps. Black arrows show horizontal vectors. Black circle shows latitude and longitude coordinates. (d–f) Horizontal velocity inversion uncertainty maps. (g–i) Vertical velocity maps for the three landslides. (j–l) Vertical velocity inversion uncertainty maps. Negative values correspond to vertically downward motion. Thick blue lines show the approximate location of the river channel at the toe of each landslide with dark blue arrows showing water flow direction.

landslide complexes. The landslide complex shown in Figure 2 is the largest landslide in our data set and is also known as the Boulder Creek landslide in several other studies (e.g., Bennett, Miller, Roering, & Schmidt, 2016; Bennett et al., 2016; Handwerger et al., 2015, 2019; Handwerger, Huang, et al., 2019; Mackey & Roering, 2011; Roering et al., 2009). We defined slumps as landslides with lower length/width aspect ratios (median = 1.57 ± 1.00, ±1 standard deviation), a strong signal of positive vertical velocity components in the toe and negative vertical velocity components in the source area, and one primary kinematic zone (Figure 2a). We defined earthflows as those with medium aspect ratios (median = 3.56 ± 1.88, ±1 standard deviation), one primary kinematic zone, and small magnitude, but mostly negative, vertical velocity components (Figure 2b). And we defined landslide complexes as those with higher aspect ratios (median = 5.13 ± 2.34, ±1 standard deviation), that are composed of multiple kinematic zones or even multiple landslides that coalesce into a single landslide mass (Figure 2c). Landslide complexes are relatively common in areas with slow-moving landslides (e.g., Cerovski-Darriau & Roering, 2016; Keefer & Johnson, 1983; Simoni et al., 2013). 33% of our inventory were classified as slumps, 31% as earthflows, and 36% as landslide complexes. The mean 3-D velocity magnitude was 0.585, 0.606, and 0.670 m/yr for slumps, earthflows, and landslide complexes, respectively.
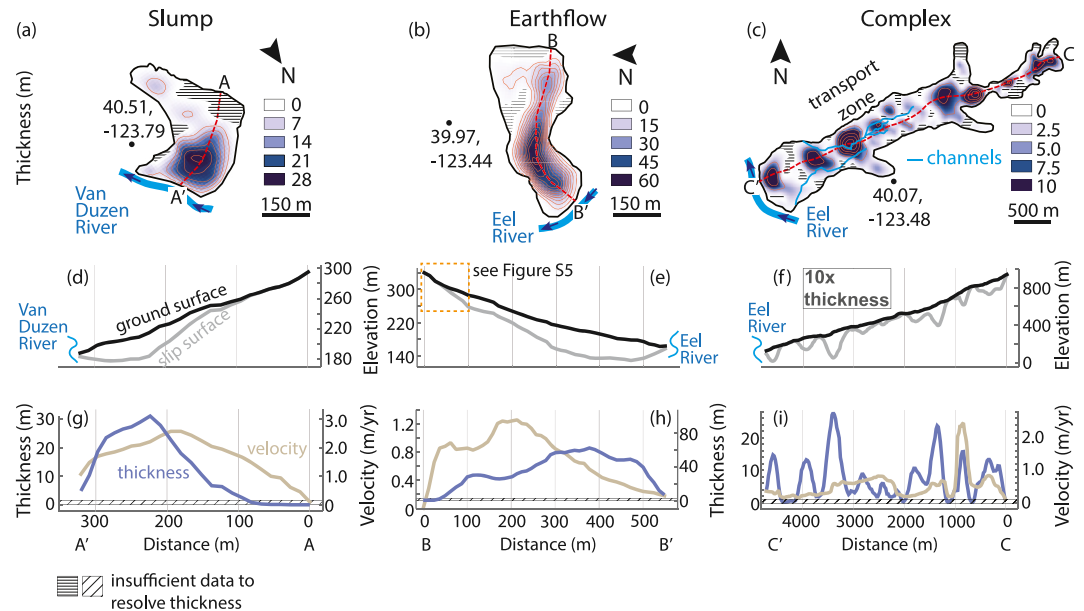
Figure 3. Landslide thickness inversions, for example, slump, earthflow, and landslide complex. (a–c) Landslide thickness maps. Thin orange lines show 5 m thickness contours. Red dashed line shows profiles plotted in (d–i). Black dots show latitude and longitude coordinates. Thick blue lines show rivers and thin blue lines show deep channels incised into the landslide body. (d–f) Ground surface and slip surface elevation profiles. Dashed orange rectangle in (e) shows location of landslide headscarp in Figure S5. In subplot (f), the results of thickness inversion are vertically exaggerated by a factor of 10 relative to the elevation profile. (g–i) Landslide thickness and 3-D velocity magnitude profiles. Hachures (a–c) and (g–i) identify areas with insufficient data to resolve thickness.

3.2. Thickness, Volume, and Geometric Scaling Relations

The nonuniform kinematic patterns exhibited by these landslides are also reflected in their inferred subsurface geometry (Figure 3). We find that the thickness of each landslide varies spatially and can vary by tens of meters within the landslide boundaries. The slip surfaces are generally concave-up, but are rough and irregular in places, especially for landslide complexes. The mean active thickness of the individual landslides ranged from 0.4 to 22.4 m, and the maximum active thickness ranged from 2.25 to 89.6 m. The mean, median, minimum, maximum, and standard deviation active thickness for each landslide are reported in Table S3.

We calculated the minimum thickness uncertainty from uncertainties in the data in vector *b* following standard inverse theory for a sample of seven landslides representing the variety of style, size, and shape found in the study population (supporting information). We found that minimum thickness uncertainty increased with landslide size (Figure S3), ranging from ± 1.5 to ± 3.8 m from the smallest to largest landslide sampled. To reduce computation time, we estimated the minimum thickness uncertainty for each landslide using a power function (Figure S3d) and propagated these uncertainties into the landslide volume calculations (Table S3).

Next, we describe our thickness inversion results for the three example types of landslides shown in Figure 2. We note again that these landslides represent their subgroups to first order. The example slump has one primary deep zone and the slip surface has a concave-up profile (Figure 3a). The slope of the slip surface deviates from the ground surface and is steeper near the headscarp and gentler near the toe. Some areas within the head of the landslide are inferred to have no active thickness because the values of *b* (Equation 4) are slightly negative near the headscarp (Figure S4). For *b* to be negative, the divergence of the horizontal landslide flux (first term on the right-hand side of Equation 3) must also be negative, which requires the landside thickness to decrease in the direction of movement. This is not physically possible because the landslide thickness is by definition zero at the headscarp, so an inferred thickness of zero minimizes the misfit there.

The example earthflow generally has a concave-up slip surface with some irregular bumps (Figure 3b). The slip surface more closely mimics the ground surface in the main transport zone; however, there are some low thickness zones near the headscarp and landslide margins that result from negative b values (Figure S4). Lastly, the example landslide complex (Boulder Creek landslide complex) has several different active zones, each with an alternating concave-up and convex-up slip surface profile (Figure 3c). The landslide slip surface is rough and irregular over the length of the entire landslide, but each deep zone generally corresponds to the different kinematic units that comprise the landslide complex (Figure 2c). This large landslide has several areas that do not have a resolvable active thickness. These patches with low active thickness result from low velocity zones (i.e., the landslide toe) and the same characteristics of the velocity field described for the example slump and earthflow (Figure S4). Patches with negative b values must have negative flux divergence, which tends to force the inferred thickness to decrease in the direction of movement at those locations.

Landslide zones with approximately zero inferred thickness should correspond to parts of landslides that are not currently active, however, as shown in Figure 3, we also observed low thickness zones in areas with detectable landslide motion. These low thickness areas in our inversions are likely a consequence of issues related to our landslide mapping, noisy velocity or slope data, or violations of the conservation of volume assumptions (e.g., nonuniform landslide density), and are better interpreted as zones where thickness is undefined, rather than where thickness is low. Because it is not possible to independently identify the exact cause of the negative b values that result in low thickness zones with our data set, we exclude these low thickness zones (<0.1 m) from our analyses since the thickness is not determined there. We selected this threshold because it characterizes the typical thin soil depth in the Central Belt Franciscan mélange (Hahm et al., 2019). We find these areas typically correspond to regions near the landslide margins for slumps and earthflows, but are scattered throughout the body of larger landslide complexes, downflow from regions with negative b values (Figure 3). After excluding the low thickness zones, the mean active thickness of the individual landslides ranged from 1.06 to 25.4 m, which, as expected, is higher than the mean thickness range including the low thickness zones (0.4–22.4 m). For the remainder of the paper, we will report landslide metrics with these low thickness zones excluded and will report metrics including the low thickness zones in Table S3.

Although we do not have borehole data to confirm our thickness estimates, we used the topography to verify the inferred slip surface elevation in several cases. Figure S5 shows the example earthflow has a clear headscarp that can be used to trace the sliding surface underneath the ground surface. The extension of the headscarp slip surface under the landslide provides confirmation that the inversion is approximating the slip surface elevation correctly. Figure S6 shows another slow-moving landslide that has filled into a pre-existing valley. Transects across this landslide show the ground surface of the filled-in valley and that the slip surface has the shape of the preexisting valley, providing additional confirmation that our inversions are approximating the slip surfaces correctly. In addition, we compared our thickness inversions to thickness estimates from lidar. Mackey and Roering (2011) used lidar to measure the toe height at the channel interface for dozens of landslides in the Eel River catchment, which is assumed to be minimum thickness estimates at those locations. Of those landslides, 10 (including slumps, earthflows, and complexes) can be used to make comparisons with our data set. We found overall good agreement between the landslide toe thickness estimated from lidar and from our inversions (Figure 4).

Using our thickness inversions for each landslide, we estimate that the individual landslide volumes range from 7.012×10^3 to 9.747×10^6 m^3 (Figure 5 and Table S3). Figure 5 also shows the distribution of mean thickness, area, and volume for each landslide type. Slumps are the smallest landslide type with a median thickness of 5.49 ± 2.99 m (± 1 standard deviation), median area of $2.71 \pm 2.05 \times 10^4$ m^2, and median volume of $1.53 \pm 1.88 \times 10^5$ m^3. Earthflows are medium sized with an inventory median thickness of 6.99 ± 5.33 m, median area of $4.99 \pm 3.26 \times 10^4$ m^2, and median volume of $2.87 \pm 5.36 \times 10^5$ m^3. And landslide complexes are the largest landslides, with a median thickness of 8.05 ± 4.34 m, median area of $1.58 \pm 3.46 \times 10^5$ m^2, and median volume of $1.22 \pm 2.19 \times 10^6$ m^3.

We fit a power function to the volume-area to characterize the geometric scaling relations (Equation 5a) for these slow-moving landslides. We also compared our inventory to a worldwide inventory of soil, undifferentiated, and bedrock landslides compiled by Larsen et al. (2010). We find that the slow-moving landslides
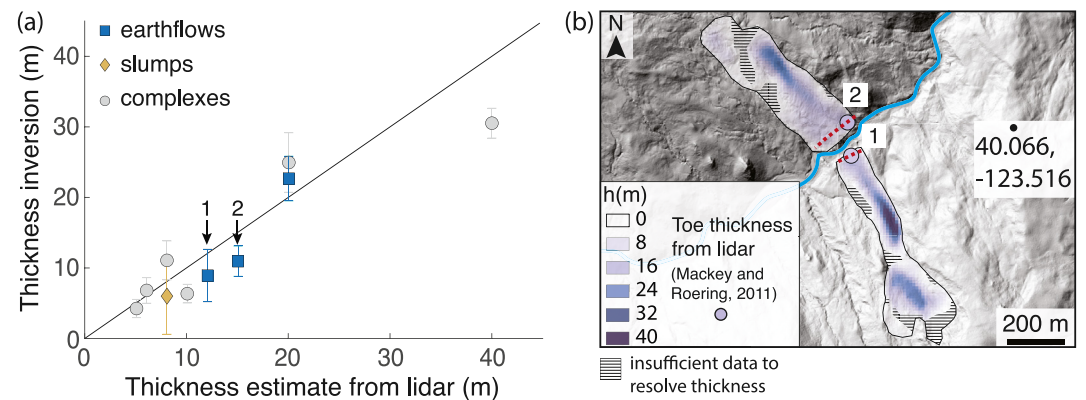
Figure 4. Landslide toe thickness estimates from lidar compared to inverted toe thickness estimates. (a) Colored symbols show inverted thickness compared to lidar estimates for 10 slumps, earthflows, and landslide complexes. We calculated the inverted toe thickness from profiles extracted across the toes and show the mean and standard deviation with error bars. Black line shows 1-to-1 line. (b) Two example landslide thickness maps draped on a lidar hillshade. Labels 1 and 2 correspond to the data points shown in (a). Hachures show zones with insufficient data to resolve thickness. Blue line shows the river channel. Red dashed line shows the profile line used to calculate toe thickness from the inversion. Toe thickness from Mackey and Roering (2011) is shown by the colored circles with black outline.

in the northern California Coast Ranges are larger in both area and volume than most soil landslides, but smaller than the largest bedrock landslides around the world (Figure 5). The best fit volume-area power function exponent (with 95% confidence) for our inventory was $\gamma = 1.306$ (1.213, 1.399) (Figure 5). We observed an apparent break in the slope of the volume-area relation for the largest landslides in our inventory with area $> 10^5$ m^2. To further investigate this break in slope, we also fit volume-area scaling as a function of landslide type and find that the break in slope is primarily associated with the landslide complexes. By fitting a power function to each landslide type, we find slumps $\gamma_S = 1.493$ (1.224, 1.762), earthflows $\gamma_{Ef} = 1.535$ (1.273, 1.796), and complexes $\gamma_C = 1.172$ (0.9858, 1.357). Although these parameters are not statistically distinct at the 95% confidence level, the fact that γ_S and γ_{Ef} overlap more with each other than with γ_C supports the argument that the break in slope is likely related to landslide type. We report all of the geometric scaling parameters in Table S4.

In addition, we calculated the thickness-area scaling relations using the mean thickness (Equation 5b) to represent each landslide (Figure 5). We compared these scaling relations to point based estimates (lidar) and measurements (boreholes) of landslide thickness for slow-moving landslides in the Eel River catchment, northern California Coast Ranges (Mackey & Roering, 2011) and the Reno River catchment, Apennines, Italy (Simoni et al., 2013). The best fit thickness-area power function exponent (with 95% confidence) for the inventory $\zeta = 0.3058$ (0.2129, 0.3987), indicating a weak increase in mean thickness with area for the inventory as a whole. We also fit thickness-area scaling as a function of landslide type and find slumps $\zeta_S = 0.4926$ (0.2236, 0.7615), earthflows $\zeta_{Ef} = 0.5348$ (0.2734, 0.7963), and for landslide complexes $\zeta_C = 0.1716$ (−0.0142, 0.3573). Therefore, landslide thickness significantly increases with area for slumps and earthflows (p-value = 0.0002 and 0.0006, respectively), but does not significantly vary with area for landslide complexes (p-value = 0.0694).

3.3. Frictional Strength

Using Equation 9, we back-calculated the landslide friction angle ϕ under dry and saturated conditions end members assuming nil cohesion. Additional landslide properties used in computations are listed in Table S2. The inferred friction angle ranged from ~6.8° to ~28° for dry conditions and ~13° to ~54° for saturated conditions (Table S3). Our inferred friction angles encompass friction angle values measured in the laboratory for Franciscan mélange rocks and landslide material (Figure 6). We also analyzed the friction angle as a function of landslide size and mean slope angle (Figure 6). We found a weak decreasing power-function relationship with increasing size and a linear increasing relationship with mean slope angle. The negative trend with length indicates that the largest landslides are weaker, on average, than smaller
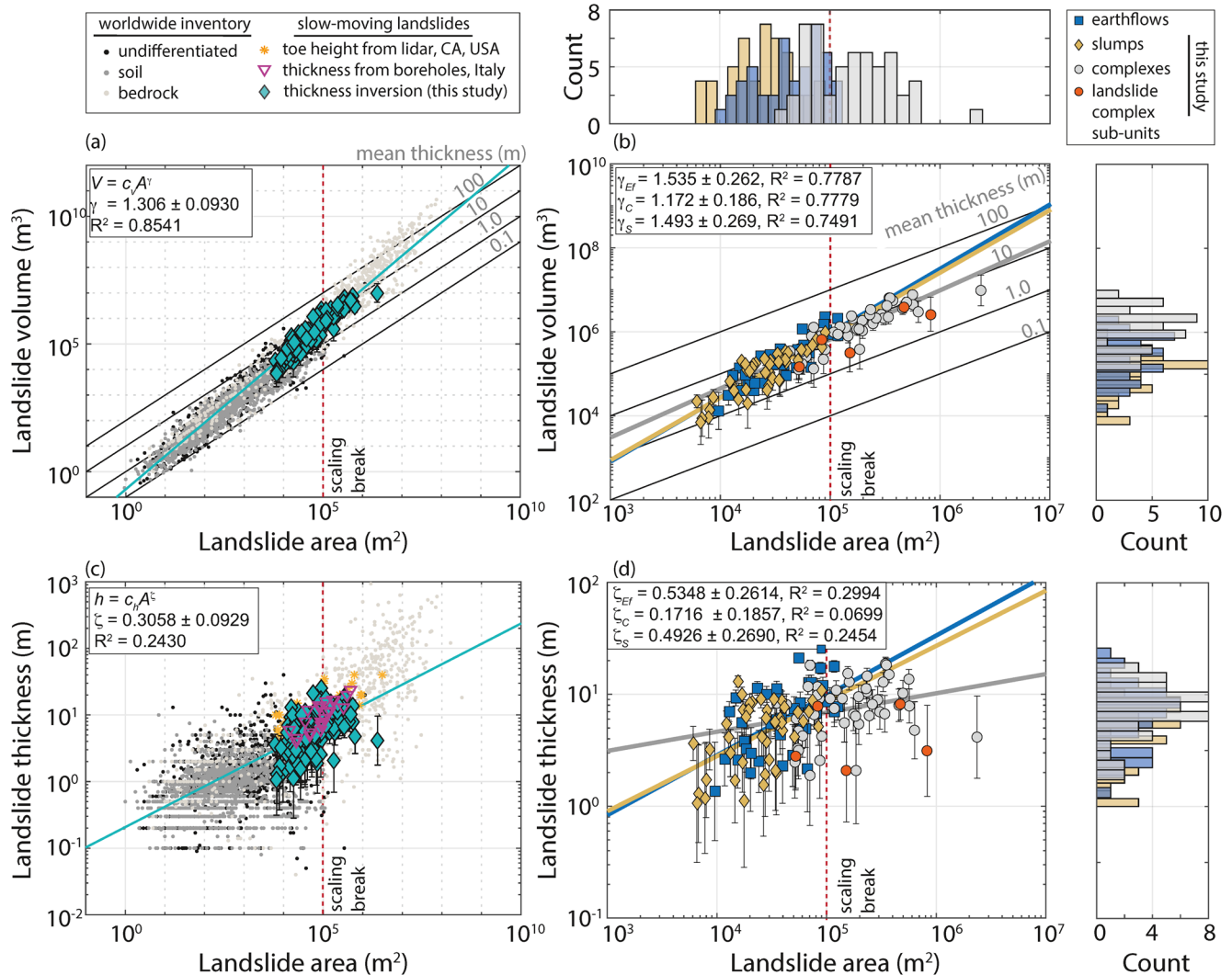
Figure 5. Landslide thickness, volume, and area geometric scaling relations. (a) Volume-area relations for our inventory and a worldwide inventory of soil, undifferentiated, and bedrock landslides (Larsen et al., 2010). (b) Volume-area relations for slumps, earthflows, and landslide complexes. (a, b) Thin diagonal black lines show volume-area for various constant mean thicknesses. (c) Thickness-area relations for our inventory (mean thickness), the worldwide inventory (Larsen et al., 2010), and slow-moving landslides in the northern California Coast Ranges (Mackey & Roering, 2011) and the Apennine mountains, Italy (Simoni et al., 2013). (d) Landslide thickness-area relations by landslide type. Orange circles in (b, d) correspond to the Boulder Creek landslide complex split into 5 smaller landslides (see Figure S7). Error bars show estimated minimum uncertainty estimates (supporting information). Red dashed vertical line shows an apparent break in scaling for the largest landslide complexes in our data set. Histograms of landslide thickness, area, and volume show the size distributions for each landslide type. All fit parameter values are in Table S4.

landslides, while the positive trend with mean slope angle indicates that landslides with gentle slopes are weaker on average. Figure 6 also shows that the weakest landslides are the large landslide complexes that have relatively gentle slope angles while slumps are the strongest and steepest landslides in our inventory.

4. Discussion

4.1. Landslide Kinematics

Our 3-D UAVSAR velocity measurements reveal 134 active slow-moving landslides in the northern California Coast Ranges moving at average rates from cm/yr to m/yr between 2016 and 2019. The 3-D velocity data confirm that the motion of these landslides is generally in the downslope direction. Many of the landslides had relatively low vertical velocities compared to their horizontal velocities that are due to the gradual slope angle (inventory mean $\sim 17°$) exhibited by these slow-moving landslides. However, we did observe
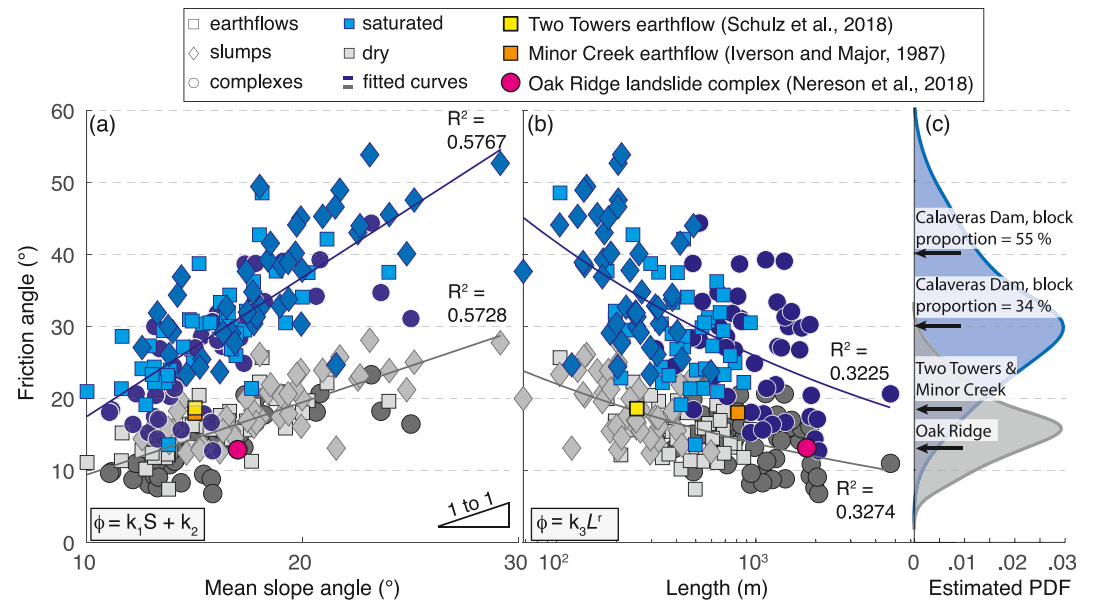
Figure 6. Inferred friction angle for dry and saturated end-members. Friction angle compared to (a) mean hillslope angle and (b) landslide length. Solid lines in (a, b) correspond to best fit linear and power function curves. For dry conditions, best fit parameters (with 95% confidence) $k_1 = 1.009$ (0.8586, 1.158), $k_2 = -0.7137$ (−3.279, 1.852), $k_3 = 57.1$ (39.66, 74.55), and $r = -0.2069$ (−0.2582, −0.1556). For wet conditions, $k_1 = 1.935$ (1.649, 2.22), $k_2 = -1.816$ (−6.699, 3.067), $k_3 = 108.4$ (74.81, 142), and $r = -0.2076$ (−0.2597, −0.1555). (c) Estimated probability density function for the full inventory. Black arrows and colored symbols show lab-based and back-calculated friction angle values for the Franciscan mélange hosted Oak Ridge (Nereson et al., 2018), Two Towers (Schulz et al., 2018), and Minor Creek landslides (Iverson, 2000; Iverson & Major, 1987) and the Calaveras Dam, which is founded on Franciscan mélange (Roadifer et al., 2009). The Calaveras Dam samples are plotted for two different block-in-matrix proportions, which are reported as percentages.

segments with vertical uplift that tended to be at the landslide toe due to the concave-up slip surface geometry, and the tendency for longitudinal shortening in the direction of motion to occur at the toe. It is possible that a component of uplift of landslide surfaces could also result from dilation or swelling (volumetric expansion), but the magnitude is small, likely on the order of a few centimeters at most (Booth et al., 2020; Delbridge et al., 2016; Iverson, 2005; Schulz et al., 2018). Including volume changes such as this in the thickness inversion may help reduce uncertainty and improve our results, especially in the zones of low thickness found in many of the landslides, but the amount of dilation or compaction occurring throughout an entire landslide and its variation is generally unknown.

Our findings agree with previous work in this region that shows that these landslides exhibit slow, spatially nonuniform downslope motion. Several of the landslides in our study area (e.g., Boulder Creek) have been moving in this manner since at least 1944 (Bennett et al., 2016; Mackey & Roering, 2011). Our findings also show that pixel offset tracking with very high resolution UAVSAR data is well-suited for monitoring landslides moving at rates >10 cm/yr. Some satellites acquire very high resolution SAR with Spotlight modes, including the German TerraSAR-X and Italian COSMO-SkyMed that could provide similar measurements (e.g., Madson et al., 2019), however these data are not open-access. Lastly, we note that there are likely active landslides or landslide zones moving below the precision of our pixel offset tracking technique (<10 cm/yr) and therefore cannot be observed with our approach. Landslides in our inventory that contain very slow-moving zones may result in unreliable thickness estimates.

4.2. Landslide Geometry

Our study is the first (to our knowledge) to apply the conservation of volume approach to invert for the thickness of multiple landslides in a given region. Previous work (Booth et al., 2020; Booth, Lamb, et al., 2013; Delbridge et al., 2016) has used the same approach to analyze individual landslides, but these

landslides occur in different regions and environmental conditions. Like these previous studies, however, we found that the active landslide thickness is variable and that the slip surfaces are rough and irregular in places. The nonuniform thickness and velocity of each landslide results in a nonuniform sediment flux, which has implications for understanding sediment motion along hillslopes (Booth et al., 2020; Guerriero et al., 2017). The shape of the slip surface likely also impacts the landslide kinematics and groundwater flow (Coe et al., 2009; Guerriero et al., 2014; Iverson & Major, 1987; Keefer & Johnson, 1983). Slip surfaces that are bumpy and rough may create additional resisting stresses that act to prevent runaway acceleration and permit long periods of slow landslide motion (Baum & Johnson, 1993; Booth et al., 2018; Leshchinsky, 2019). Investigation of tectonic faults and glaciers also shows that slip surface roughness is an important parameter that controls frictional strength (Brodsky et al., 2016; Fang & Dunham, 2013; Meyer et al., 2018).

For our thickness inversions, we assumed that the depth-averaged velocity was equal to the surface velocity (i.e., $f = 1$) for all landslides. This block on slope approximation was made to simplify our regional scale analyses. Yet the borehole data from the Two Towers landslide shows that $f \sim 0.96$ (Figure S1). While changing f uniformly for each landslide does not alter the spatial pattern of thickness or scaling exponents, it does impact the magnitude of the thickness and therefore the volume. Setting $f = 0.96$ would cause a 4% increase in the inferred thickness and volume of each landslide ($h \sim 1/f$) (Table S3). More work is needed to better constrain the depth-averaged velocity for individual landslides in our field area, particularly to see if f differs with landslide type. Nonetheless, our findings indicate that most of the sliding surfaces are deep-seated (mean thickness for inventory ~ 7.2 m) and thus are expected to lie within the unweathered Central Belt Franciscan mélange bedrock (Hahm et al., 2019). Therefore, the slow-moving landslides in the northern California Coast Ranges can be classified as bedrock landslides.

Using our landslide inventory, we developed new volume-area and thickness-area geometric scaling relations for slow-moving landslides. Geometric scaling relations are particularly useful for slow-moving landslides because these landslides rarely (if ever) evacuate hillslopes, or create clear scars or deposits that can be easily measured. As a result, most measurements of landslide thickness come from isolated boreholes, which are logistically challenging and expensive to install, and are difficult to extrapolate over an entire landslide. Our results provide best fit volume-area power function exponents ($\gamma \sim 1.2$–1.5) that are comparable to power function exponents for bedrock and soil landslides (Bunn et al., 2020a; Guzzetti et al., 2009; Larsen et al., 2010). Recent work by Bunn et al. (2020a) found that deep-seated bedrock landslides in Oregon, USA had $\gamma_{bedrock} \sim 1.4$–1.6. Analysis of a worldwide landslide inventory by Larsen et al (2010) showed that soil landslides had a $\gamma_{soil} \sim 1.1$–1.3, while bedrock landslides had $\gamma_{bedrock} \sim 1.3$–1.6.

In addition, our best fit thickness-area scaling power exponents ($\zeta \sim 0.17$–0.53) are also comparable (with a wide range) to previously published values for deep-seated landslides (Figure 4c). Bunn et al. (2020a) found $\zeta \sim 0.41$–0.58 for deep-seated bedrock landslides. Simoni et al. (2013) reported $\zeta = 0.44$ from borehole inclinometer data from 23 slow-moving landslides in the Apennine Mountains, Italy. Handwerger et al. (2013) reported $\zeta = 0.29$ derived from lidar-based estimates of landslide toe thickness from 69 landslides in the Eel River catchment, several of which are also analyzed in this study (e.g., Figure 4). Importantly, neither Simoni et al. (2013) or Handwerger et al. (2013) used large inventories (>100) or spatially extensive measurements of landslide thickness, which are especially important for slow-moving landslides with variable thicknesses. Therefore, our new scaling relationships provide the most appropriate values for deep-seated slow-moving landslides, like earthflows, and could be used to help estimate sediment flux and landslide stresses in similar areas around the world. Yet, we note that the large range of scaling exponents suggests that scaling relations should be used with caution. Applying an incorrect scaling exponent to estimate volume for landslides with unknown thickness can lead to large errors in volume calculations (Larsen et al., 2010).

Our findings show that the slow-moving landslides located in the northern California Coast Ranges have geometric scaling exponents that lie in between the soil and bedrock type landslides. However, examining the best fit power function exponents by landslide type suggests that slumps and earthflows display close to self-similar scaling ($\gamma_{self-similar} = 1.5$), which is characteristic of bedrock landslides, while landslide complexes display scaling that is characteristic of soil landslides. Figure 5b shows that the landslide complexes with the largest areas display a scaling that tends to follow a constant mean thickness. We propose that landslide complexes have scaling relations that are close to soil landslides because: 1) the mean landslide thickness is

limited by a strong layer in the mélange (and thus are similar to soil landslides that are limited by the soil thickness), or 2) that landslide complexes are an amalgamation of multiple smaller and shallower landslides. The second explanation provides a reason for why large landslide complexes tend to have multiple kinematic units (e.g., Aryal et al., 2012; Hu et al., 2020) and further emphasizes the importance of having detailed landslide maps, especially when applying geometric scaling relations (e.g., Marc & Hovius, 2015).

4.3. Thickness Inversion Challenges

The inferred thickness of many of the slow-moving landslides, in particular the landslide complexes, can be highly variable with deeper active zones and thinner or zero thickness areas that are not currently moving (Figure 3). In addition, some patches with an inferred thickness of zero occurred in areas where $b < 0$, such that a negative divergence was required to match the observations (Figure S4). These negative b values typically arose when the product of the horizontal velocity and the topographic gradient was more negative than the vertical component of the surface velocity vector (Equations 3 and 4). This situation could result from artifacts in the velocity or topographic data or from actual physical processes occurring in the landslide that would tend to increase the magnitude of the horizontal velocity, increase the magnitude of the topographic gradient, or decrease the magnitude of the vertical velocity relative to their true values, assuming conservation of volume. In particular, one plausible physical mechanism that would decrease the magnitude of v_{ud} relative to that of u_{surf} or ∇z_{surf} is dilation of landslide material as it deforms. That increase in volume would cause an additional positive vertical component to v_{ud}. Although we cannot determine whether errors in the velocity and topographic data, or actual physical mechanisms are responsible for the low inferred thickness zones, we find dilation a plausible explanation, especially near landslide headscarps, or in other zones of extension, indicating macro-scale decreases in density.

Additionally, it is important to note that the irregular thickness patterns observed in some landslides may not align with inferred thickness based on geomorphic or structural interpretations. This discrepancy is likely related to the long-lasting geomorphic imprint that slow-moving landslides have made on the landscape. Landslide surface morphology may last for decades or longer after a landslide completely stops moving (e.g., Booth et al., 2017), which can make it challenging to infer the active landslide thickness without kinematic data. Although our approach is useful for identifying the currently active portions of landslides and inferring their thickness based on volume conservation (with assumptions), it does not allow us to infer the subsurface geometry of the often larger inactive landslide body. As a result, we emphasize the need for more comparisons between ground- and remote sensing-based investigation of landslide geometry. In particular, direct comparison between numerous ground-based measurements from boreholes and structural mapping are needed to widely test the results of our remote sensing approach. Nonetheless, we find our thickness inversions are producing reasonable estimates of landslide thickness in the cases we were able to test (Figures 4, S5, and S6).

4.4. The Boulder Creek Landslide Complex

We found that the inferred active thickness for the Boulder Creek landslide complex was particularly irregular and challenging to explain based on a priori assumptions of landslide geometry. While we expect areas that are not currently active to thin, and even have zero thickness in places (e.g., parts of the landslide toe), the active transport zone on Boulder Creek also contains thin and thick patches (Figures 3c, 3f and 3i). One possible explanation for this variability is related to patches of local density changes (e.g., dilation) that could result in negative b values. In addition to these potential artifacts, another possible cause of these low thickness zones is related to the large channel network incised into the landslide (Figure 3). In some places the channel reaches depths of 15–20 m (Figure S8). Since the thickness is measured as the vertical distance from the ground surface to the inferred basal sliding surface, the predicted thickness is expected to be low in places surrounding the channel if the channel depth is similar to the landslide thickness. Our findings indicate that the channel has incised to depths that approach the predicted sliding surface in several places (Figure S8). However, the channel has not incised deeper than the landslide base because we find the channel is moving with similar velocity to the surrounding regions (Figure 2c).

The distinct kinematic zones within Boulder Creek landslide complex also indicate that smaller, faster, and possibly shallower features are superimposed on a larger, slower, and possibly deeper-seated failure (Figure 2c). If multiple failure planes are indeed present, that would violate the assumption of a constant f throughout the landslide and cause unreliable thickness estimates. Specifically, the surface velocity would be much greater than the depth-averaged velocity (i.e., f would be much smaller) within the superimposed landslide. This would systematically cause the inferred thickness to be too large near the headscarp of the superimposed landslide and too shallow near its toe, since the divergence of the surface velocity field would be much greater than the divergence of the depth-averaged velocity field at those locations. To further explore the hypothesis that the Boulder Creek landslide complex is composed of multiple smaller landslides, we delineated Boulder Creek into 5 smaller sub-landslides and performed a thickness inversion for each sub-landslide (Figure S7). While the thickness patterns are similar to the thickness inversion for the full landslide complex, the magnitude of the inferred thickness differs in some places, and the area of each landslide is smaller, which places them into the space mostly populated by earthflows on the thickness-area and volume-area plots (orange circles in Figures 5b and 5d). Some of these differences in the magnitude of the thickness estimate are due to differences in the pixel resolution of the sub-landslides (10 m pixel) and the full landslide (20 m pixel). Nonetheless, mapping landslide complexes as one large landslide results in a lower mean thickness relative to the landslide area which affects the geometric scaling relations. While more investigation is warranted, our thickness inversions have caused us to reevaluate how we think about large landslide complexes.

4.5. Landslide Strength

Our back-analysis of landslide strength suggests that there is a weak decreasing relationship between landslide size and strength and an increasing relationship between mean slope angle and strength (Figures 6 and S9). The increasing relationship between mean slope angle and friction angle was expected because steeper landslides must be stronger to maintain force balance (Equation 9). The decreasing relationship between landslide size and friction angle is notable and intriguing. We hypothesize that larger landslides are weaker than smaller landslides because of strength heterogeneity in the Franciscan mélange bedrock and the increased likelihood of incorporating weak material within larger volumes. Laboratory measurements of the strength of the Franciscan mélange rocks have shown that the proportion of the blocks hosted in the argillaceous matrix controls the overall rock strength (Roadifer et al., 2009) (Figure 6). This implies that larger landslides may have a decreased proportion of blocks, which are not uniformly distributed, and are therefore controlled by the weak argillaceous matrix.

Scale-dependent strength has also been observed along other landslides and faults. Brodsky et al. (2016) suggested that faults are weaker at large spatial scales because they encompass larger weak zones. A recent study by Bunn et al. (2020b) found that the inferred shear strength of landslides decreases with increasing landslide size. They proposed that smaller landslides were stronger because they occur in cemented cohesive materials and larger landslides were in a residual state. Although we assumed nil cohesion to back-calculate the residual frictional strength of the active landslides, it is likely that cohesion is important in controlling the initial landslide failure due to the high-clay content of the Central Belt Franciscan mélange.

Our inferred friction angles also depend on wetness conditions. Due to the high seasonal rainfall in the northern California Coast Ranges, these slow-moving landslides are typically saturated (or nearly saturated) during the wet season and partially saturated or dry during the dry season (Hahm et al., 2019; Iverson & Major, 1987; Schulz et al., 2018). Direct comparison with friction angle values measured in the laboratory and back-calculated for Franciscan mélange rocks and landslide materials provides some insight into our findings. For saturated conditions, we find that the inferred friction angles for medium to large earthflows and landslide complexes overlap the measured friction values from the Two Towers earthflow (Schulz et al., 2018), Minor Creek earthflow (Iverson & Major, 1987), and Oakridge landslide complex (Nereson et al., 2018). The majority of the smaller slumps have saturated friction angles that are significantly higher than these three landslides. The saturated friction values for smaller slumps, earthflows, and landslide complexes have more overlap with measured rock friction values that depend on the block-in-matrix proportion (Roadifer et al., 2009). Interestingly, the dry friction angles for all landslide types have more overlap with lab-based friction measurements for the landslides. Yet, it is unlikely that most of these landslides,

especially the larger landslides, become completely dry. Instead, the true landslide-scale friction angle values likely lie somewhere between our inferred values for saturated and dry conditions.

We suggest that some of these differences between lab-based and inferred friction angles may be attributed to commonly observed differences in laboratory- and field-scale measurements that are often related to large scale spatial heterogeneity in the field (e.g., Marone, 1998; Van Asch et al., 2007). In addition, our assumption of nil cohesion can partially explain the higher friction values for saturated conditions (Bunn et al., 2020b). The additional strength imparted by cohesion would act to reduce the inferred friction angle values to maintain equilibrium (Equation 9). We assumed nil cohesion because the landslides have moved significantly over the study period (and likely much longer), but it is likely that cohesion is important for the clay-rich landslide material and future work needs to better account for temporal changes in cohesion, which may be especially important for landslides that completely stop moving during dry periods. While the large spread of inferred friction values makes it difficult to identify a single representative value for slow-moving landslides in the northern California Coast Ranges, our results further highlight the heterogeneous nature of the Central Belt Franciscan mélange lithologic unit. Similar to the recent findings of Bunn et al. (2020b), our findings also suggest that landslide type, mean slope angle, and wetness conditions may provide some first-order information on relative landslide strength at the regional scale. Furthermore, our findings have implications for understanding landscape evolution and agree with previous work that shows that over geomorphic timescales, we generally expect to find steeper hillslopes where hillslope materials are stronger (e.g., Korup et al., 2007; Roering et al., 2015). More work is needed to understand our findings in the context of landscape evolution because the currently active landslides are just the most recent snapshot of the landscape, and the slopes they occur on have probably been shaped by numerous previous generations of similar landslides (e.g., Mackey & Roering, 2011; Roering et al., 2015).

4.6. What Controls the Size of Slow-Moving Landslides?

Landslide size is set by the landslide mechanical properties, slope geometry, and environmental conditions. For most landslides, the maximum size is typically limited to the maximum hillslope size, such that the landslide length does not exceed the hillslope length. The landslide thickness is typically set by the location of a weak layer beneath the ground surface, or at a depth where there are changes in strength and permeability, such as the soil to bedrock transition or the bottom of the critical zone (i.e., the zone that extends from the ground surface down to unweathered bedrock) (Booth, Roering, et al., 2013; Larsen et al., 2010; Milledge et al., 2014). Using a 3-D slope stability model for shallow soil landslides that accounts for the forces acting on the landslide basal slip surface, lateral margins, and passive/active wedges at the toe/head, Milledge et al. (2014) found that the critical area and depth that can fail as a landslide depends on the topography, pore-water pressure, and landslide material properties, including density, cohesion, and friction angle. We note that their modeled landslides have less complex geometries than the landslides in our inventory. In their model the pore-water pressure plays a fundamental role in determining the critical landslide size and failure depth, such that higher pore-water pressures decrease the critical size required for failure. Large landslides therefore occur when high pore pressures are reached over a correspondingly large spatial area. At our northern California Coast Range study site, the relatively thin, but laterally extensive critical zone that is often saturated during the wet season (Hahm et al., 2019), may promote laterally extensive landslides by elevating the water table height simultaneously over large areas.

Milledge et al. (2014)'s model also predicts that landslide thickness should increase as the square root of the landslide area and that the failure depth sets the minimum landslide area. Our best fit thickness-area scaling exponents for slumps and earthflows are close to a square root scaling (exponents ∼0.5 with large 95th confidence intervals). Our results also suggest that the landslide thickness controls the minimum area, but does not bound its maximum size. Instead, slow-moving landslides can continue to grow in area by becoming a landslide complex consisting of multiple, connected, sublandslides without becoming significantly deeper on average. Large landslide complexes can occupy multiple hillslopes, and fill valleys and catchments such that their size may exceed the typical hillslope size, in contrast to landslides that fully evacuate their hillslopes (e.g., Jeandet et al., 2019). Thus, it seems that the catchment size sets the maximum area for slow-moving landslides. Our thickness inversion results also indicate that large landslides are weaker than small landslides. This finding may indicate that large landslides become large by incorporating weak

material. It is possible that the largest landslides grow over time and take decades to develop (e.g., Mackey & Roering, 2011). As many of our landslide complexes seem to be composed of several smaller sublandslides or kinematic zones, it is possible that these features have connected through time as slip surfaces propagate along the slope.

5. Conclusions

We measured the 3-D surface velocity of more than one hundred slow-moving landslides in the northern California Coast Ranges with data from the NASA/JPL UAVSAR. We used volume conservation techniques to infer the active thickness, volume, and strength of each landslide. The thickness of each landslide is variable and can vary by tens of meters sometimes resulting in an irregular slip surface geometry. Volume-area geometric scaling relations suggest that these landslides have similarities to both soil and bedrock landslides around the world. Although their failure planes are likely hosted in unweathered bedrock, their thickness seems to be limited, producing a scaling similar to soil landslides for the largest landslide complexes. The inferred residual friction angles are also scale-dependent, like faults, such that large landslide complexes tend to be weaker than small landslides such as slumps. This decrease in inferred friction angle with landslide size is likely because larger landslides are composed of larger proportions of weak material. Our study represents the first to use the conservation of volume approach for numerous landslides occurring under the same environmental conditions. Our results provide key insights into the subsurface geometry and strength that control the behavior of slow-moving landslides. Our work shows how state-of-the-art remote sensing techniques can be used to better understand landslide processes for hazards and to quantify their contribution to landscape evolution.

Data Availability Statement

Landslide geometry data used in this study are listed in the references: Larsen et al. (2010), Mackey and Roering (2011), Simoni et al. (2013) and are included in the figures. Borehole thickness data at the Two Towers landslide is in reference: Schulz et al. (2018). Lidar digital elevation models are provided by OpenTopography and may be downloaded online (http://www.opentopography.org). OpenTopography lidar data acquisition and processing was completed by the National Center for Airborne Laser Mapping (NCALM; http://ncalm.cive.uh.edu/). NCALM funding was provided by NSF's Division of Earth Sciences, Instrumentation, and Facilities Program EAR-1043051. Topographic data are also provided by the German Aerospace Center (DLR) under data proposal DEM GEOL1478 awarded to A. L. Handwerger. To acquire these data, proposals may be submitted to the DLR online (https://tandemx-science.dlr.de/). NASA/JPL UAVSAR data used in this study are freely available and may be downloaded through their website (https://uavsar.jpl.nasa.gov/).

References

Aryal, A., Brooks, B. A., & Reid, M. E. (2015). Landslide subsurface slip geometry inferred from 3D surface displacement fields. *Geophysical Research Letters*, *42*(5), 1411–1417. https://doi.org/10.1002/2014GL062688

Aryal, A., Brooks, B. A., Reid, M. E., Bawden, G. W., & Pawlak, G. R. (2012). Displacement fields from point cloud data: Application of particle imaging velocimetry to landslide geodesy. *Journal of Geophysical Research*, *117*, F01029. https://doi.org/10.1029/2011JF002161

Baum, R. L., & Johnson, A. M. (1993). *Steady movement of landslides in fine-grained soils: A model for sliding over an irregular slip surface*. U.S. Geological Survey Bulletin.

Bennett, G. L., Miller, S. R., Roering, J. J., & Schmidt, D. A. (2016). Landslides, threshold slopes, and the survival of relict terrain in the wake of the Mendocino Triple Junction. *Geology*, *44*(5), 363–366. https://doi.org/10.1130/G37530.1

Bennett, G. L., Roering, J. J., Mackey, B. H., Handwerger, A. L., Schmidt, D. A., & Guillod, B. P. (2016). Historic drought puts the brakes on earthflows in Northern California. *Geophysical Research Letters*, *43*(11), 5725–5731. https://doi.org/10.1002/2016GL068378

Bessette-Kirton, E. K., Coe, J. A., & Zhou, W. (2018). Using stereo satellite imagery to account for ablation, entrainment, and compaction in volume calculations for rock avalanches on glaciers: Application to the 2016 Lamplugh rock avalanche in Glacier Bay National Park, Alaska. *Journal of Geophysical Research: Earth Surface*, *123*(4), 622–641. https://doi.org/10.1002/2017JF004512

Booth, A. M., LaHusen, S. R., Duvall, A. R., & Montgomery, D. R. (2017). Holocene history of deep-seated landsliding in the North Fork Stillaguamish River valley from surface roughness analysis, radiocarbon dating, and numerical landscape evolution modeling. *Journal of Geophysical Research: Earth Surface*, *122*(2), 456–472. https://doi.org/10.1002/2016JF003934

Booth, A. M., Lamb, M. P., Avouac, J.-P., & Delacourt, C. (2013). Landslide velocity, thickness, and rheology from remote sensing: La Clapière landslide, France. *Geophysical Research Letters*, *40*(16), 4299–4304. https://doi.org/10.1002/grl.50828

Booth, A. M., McCarley, J., Hinkle, J., Shaw, S., Ampuero, J.-P., & Lamb, M. P. (2018). Transient reactivation of a deep-seated landslide by undrained loading captured with repeat airborne and terrestrial lidar. *Geophysical Research Letters*, *45*(10), 4841–4850. https://doi.org/10.1029/2018GL077812

Booth, A. M., McCarley, J. C., & Nelson, J. (2020). Multi-year, three-dimensional landslide surface deformation from repeat lidar and response to precipitation: Mill Gulch earthflow, California. *Landslides*, *17*, 1283–1296. https://doi.org/10.1007/s10346-020-01364-z

Booth, A. M., Roering, J. J., & Rempel, A. W. (2013). Topographic signatures and a general transport law for deep-seated landslides in a landscape evolution model. *Journal of Geophysical Research: Earth Surface*, *118*(2), 603–624. https://doi.org/10.1002/jgrf.20051

Brodsky, E. E., Kirkpatrick, J. D., & Candela, T. (2016). Constraints from fault roughness on the scale-dependent strength of rocks. *Geology*, *44*(1), 19–22. https://doi.org/10.1130/G37206.1

Bunn, M., Leshchinsky, B., & Olsen, M. J. (2020a). Estimates of three-dimensional rupture surface geometry of deep-seated landslides using landslide inventories and high-resolution topographic data. *Geomorphology*, *367*, 107332. https://doi.org/10.1016/j.geomorph.2020.107332

Bunn, M., Leshchinsky, B., & Olsen, M. J. (2020b). Geologic trends in shear strength properties inferred through three-dimensional back-analysis of landslide inventories. *Journal of Geophysical Research: Earth Surface*, *125*, e2019JF005461. https://doi.org/10.1029/2019JF005461

Cerovski-Darriau, C., & Roering, J. J. (2016). Influence of anthropogenic land-use change on hillslope erosion in the Waipaoa River Basin, New Zealand. *Earth Surface Processes and Landforms*, *41*(15), 2167–2176. https://doi.org/10.1002/esp.3969

Coe, J. A., McKenna, J. P., Godt, J. W., & Baum, R. L. (2009). Basal-topographic control of stationary ponds on a continuously moving landslide. *Earth Surface Processes and Landforms*, *34*(2), 264–279. https://doi.org/10.1002/esp.1721

Cruden, D. M., & Varnes, D. J. (1996). *Landslides: Investigation and mitigation. Chapter 3-landslide types and processes*. Transportation Research Board Special Report.

Delbridge, B. G., Bürgmann, R., Fielding, E., Hensley, S., & Schulz, W. H. (2016). Three-dimensional surface deformation derived from airborne interferometric UAVSAR: Application to the Slumgullion Landslide. *Journal of Geophysical Research: Solid Earth*, *121*(5), 3951–3977. https://doi.org/10.1002/2015JB012559

Fang, Z., & Dunham, E. M. (2013). Additional shear resistance from fault roughness and stress levels on geometrically complex faults. *Journal of Geophysical Research: Solid Earth*, *118*(7), 3642–3654. https://doi.org/10.1002/jgrb.50262

Fialko, Y., Simons, M., & Agnew, D. (2001). The complete (3-D) surface displacement field in the epicentral area of the 1999 Mw7. 1 Hector Mine earthquake, California, from space geodetic observations. *Geophysical Research Letters*, *28*(16), 3063–3066. https://doi.org/10.1029/2001GL013174

Fielding, E. J., Liu, Z., Stephenson, O. L., Zhong, M., Liang, C., Moore, A., et al. (2020). Surface deformation related to the 2019 M w 7.1 and 6.4 Ridgecrest Earthquakes in California from GPS, SAR Interferometry, and SAR pixel offsets. *Seismological Research Letters*, *91*, 2035–2046. https://doi.org/10.1785/0220190302

Grant, M., & Boyd, S. (2014). *CVX: Matlab software for disciplined convex programming, version 2.1*. Retrieved from http://cvxr.com/cvx

Guerriero, L., Bertello, L., Cardozo, N., Berti, M., Grelle, G., & Revellino, P. (2017). Unsteady sediment discharge in earth flows: A case study from the Mount Pizzuto earth flow, southern Italy. *Geomorphology*, *295*, 260–284. https://doi.org/10.1016/j.geomorph.2017.07.011

Guerriero, L., Coe, J. A., Revellino, P., Grelle, G., Pinto, F., & Guadagno, F. M. (2014). Influence of slip-surface geometry on earth-flow deformation, Montaguto earth flow, southern Italy. *Geomorphology*, *219*(0), 285–305. http://dx.doi.org/10.1016/j.geomorph.2014.04.039

Guzzetti, F., Ardizzone, F., Cardinali, M., Rossi, M., & Valigi, D. (2009). Landslide volumes and landslide mobilization rates in Umbria, central Italy. *Earth and Planetary Science Letters*, *279*(3–4), 222–229. https://doi.org/10.1016/j.epsl.2009.01.005

Hahm, W. J., Rempe, D. M., Dralle, D. N., Dawson, T. E., Lovill, S. M., Bryk, A. B., et al. (2019). Lithologically controlled subsurface critical zone thickness and water storage capacity determine regional plant community composition. *Water Resources Research*, *55*(4), 3028–3055. https://doi.org/10.1029/2018WR023760

Handwerger, A. L., Fielding, E. J., Huang, M.-H., Bennett, G. L., Liang, C., & Schulz, W. H. (2019). Widespread initiation, reactivation, and acceleration of landslides in the northern California Coast Ranges due to extreme rainfall. *Journal of Geophysical Research: Earth Surface*, *124*(7), 1782–1797. https://doi.org/10.1029/2019JF005035

Handwerger, A. L., Huang, M.-H., Fielding, E. J., Booth, A. M., & Bürgmann, R. (2019). A shift from drought to extreme rainfall drives a stable landslide to catastrophic failure. *Scientific Reports*, *9*(1), 1569. https://doi.org/10.1038/s41598-018-38300-0

Handwerger, A. L., Roering, J. J., & Schmidt, D. A. (2013). Controls on the seasonal deformation of slow-moving landslides. *Earth and Planetary Science Letters*, *377*, 239–247. https://doi.org/10.1016/j.epsl.2013.06.047

Handwerger, A. L., Roering, J. J., Schmidt, D. A., & Rempel, A. W. (2015). Kinematics of earthflows in the Northern California Coast Ranges using satellite interferometry. *Geomorphology*, *246*, 321–333. https://doi.org/10.1016/j.geomorph.2015.06.003

Hu, X., Bürgmann, R., Schulz, W. H., & Fielding, E. J. (2020). Four-dimensional surface motions of the Slumgullion landslide and quantification of hydrometeorological forcing. *Nature Communications*, *11*(1), 1–9. https://doi.org/10.1038/s41467-020-16617-7

Hungr, O. (1987). An extension of Bishop's simplified method of slope stability analysis to three dimensions. *Geotechnique*, *37*(1), 113–117. https://doi.org/10.1680/geot.1987.37.1.113

Hungr, O., Leroueil, S., & Picarelli, L. (2014). The Varnes classification of landslide types, an update. *Landslides*, *11*(2), 167–194. https://doi.org/10.1007/s10346-013-0436-y

Hungr, O., Salgado, F., & Byrne, P. (1989). Evaluation of a three-dimensional method of slope stability analysis. *Canadian Geotechnical Journal*, *26*(4), 679–686. https://doi.org/10.1139/t89-079

Iverson, R. M. (2000). Landslide triggering by rain infiltration. *Water Resources Research*, *36*(7), 1897–1910. https://doi.org/10.1029/2000WR900090

Iverson, R. M. (2005). Regulation of landslide motion by dilatancy and pore pressure feedback. *Journal of Geophysical Research*, *110*, F000268. https://doi.org/10.1029/2004JF000268

Iverson, R. M., & Major, J. J. (1987). Rainfall, ground-water flow, and seasonal movement at Minor Creek landslide, northwestern California: Physical interpretation of empirical relations. *Geological Society of America Bulletin*, *99*(4), 579–594. https://doi.org/10.1130/0016-7606(1987)99<579:RGFASM>2.0.CO;2

Jayko, A., Blake, M., McLaughlin, R., Ohlin, H., Ellen, S., & Kelsey, H. (1989). *Reconnaissance geologic map of the Covelo 30-by 60-Minute Quadrangle*. Northern California: U.S. Geological Survey Miscellaneous Field Investigation Map MF-2001, Scale, 1(100), 000. Retrieved from https://doi.org/10.3133/mf2001

Jeandet, L., Steer, P., Lague, D., & Davy, P. (2019). Coulomb mechanics and relief constraints explain landslide size distribution. *Geophysical Research Letters*, *46*, 4258–4266. https://doi.org/10.1029/2019GL082351

Jennings, C. W., Strand, R. G., & Rogers, T. H. (1977). *Geologic map of California*. California Division of Mines and Geology, scale 1:750,000.

Keefer, D. K., & Johnson, A. M. (1983). *Earth flows: Morphology, mobilization, and movement*. Washington, DC: United States Government Printing Office. No 1264. https://doi.org/10.3133/pp1264

Kelsey, H. M. (1978). Earthflows in Franciscan mélange, Van Duzen River basin, California. *Geology*, *6*(6), 361–364. https://doi.org/10.1130/0091-7613(1978)6<361:EIFMVD>2.0.CO;2

Korup, O., Clague, J. J., Hermanns, R. L., Hewitt, K., Strom, A. L., & Weidinger, J. T. (2007). Giant landslides, topography, and erosion. *Earth and Planetary Science Letters*, *261*(3–4), 578–589. https://doi.org/10.1016/j.epsl.2007.07.025

Lacroix, P., Dehecq, A., & Taipe, E. (2020). Irrigation-triggered landslides in a Peruvian desert caused by modern intensive farming. *Nature Geoscience*, *13*(1), 56–60. https://doi.org/10.1038/s41561-019-0500-x

Lacroix, P., Handwerger, A. L., & Bièvre, G. (2020). Life and death of slow-moving landslides. *Nature Reviews Earth & Environment*, *1*, 404–419. https://doi.org/10.1038/s43017-020-0072-8

Larsen, I. J., Montgomery, D. R., & Korup, O. (2010). Landslide erosion controlled by hillslope material. *Nature Geoscience*, *3*(4), 247–251. https://doi.org/10.1038/ngeo776

Legros, F. (2002). The mobility of long-runout landslides. *Engineering Geology*, *63*(3–4), 301–331. https://doi.org/10.1016/S0013-7952(01)00090-4

Leshchinsky, B. (2019). Quantifying the influence of failure surface asperities on the basal shear resistance of translational landslides. *Landslides*, *16*(7), 1375–1383. https://doi.org/10.1007/s10346-019-01185-9

Mackey, B. H., & Roering, J. J. (2011). Sediment yield, spatial characteristics, and the long-term evolution of active earthflows determined from airborne LiDAR and historical aerial photographs, Eel River, California. *Geological Society of America Bulletin*, *123*(7–8), 1560–1576. https://doi.org/10.1130/B30306.1

Mackey, B. H., Roering, J. J., & McKean, J. (2009). Long-term kinematics and sediment flux of an active earthflow, Eel River, California. *Geology*, *37*(9), 803–806. https://doi.org/10.1130/G30136A.1

Madson, A., Fielding, E., Sheng, Y., & Cavanaugh, K. (2019). High-resolution spaceborne, airborne and in situ landslide kinematic measurements of the Slumgullion landslide in Southwest Colorado. *Remote Sensing*, *11*(3), 265. https://doi.org/10.3390/rs11030265

Malet, J.-P., Maquaire, O., & Calais, E. (2002). The use of global positioning system techniques for the continuous monitoring of landslides: Application to the Super-Sauze earthflow (Alpes-de-Haute-Provence, France). *Geomorphology*, *43*(1–2), 33–54. https://doi.org/10.1016/S0169-555X(01)00098-8

Marc, O., & Hovius, N. (2015). Amalgamation in landslide maps: Effects and automatic detection. *Natural Hazards & Earth System Sciences*, *15*, 723–733. https://doi.org/10.5194/nhess-15-723-2015

Marone, C. (1998). Laboratory-derived friction laws and their application to seismic faulting. *Annual Review of Earth and Planetary Sciences*, *26*(1), 643–696. https://doi.org/10.1146/annurev.earth.26.1.643

McLaughlin, R. J., Blake, S., Jayko, M., Irwin, A., Aalto, W., Carver, K., et al. (2000). *Geologic map of the Cape Mendocino, Eureka, garberville, and southwestern part of the Hayfork 30 X 60 Quadrangles and Adjacent Offshore Area, Northern California*. U.S. Geological Survey.

McLaughlin, R. J., Kling, S. A., Poore, R. Z., McDougall, K., & Beutner, E. C. (1982). Post-middle Miocene accretion of Franciscan rocks, northwestern California. *Geological Society of America Bulletin*, *93*(7), 595–605. https://doi.org/10.1130/0016-7606(1982)93<595:PMAOFR>2.0.CO;2

Meyer, C. R., Downey, A. S., & Rempel, A. W. (2018). Freeze-on limits bed strength beneath sliding glaciers. *Nature Communications*, *9*(1), 1–6. https://doi.org/10.1038/s41467-018-05716-1

Michel, J., Dario, C., Marc-Henri, D., Thierry, O., Marina, P. I., & Bejamin, R. (2020). A review of methods used to estimate initial landslide failure surface depths and volumes. *Engineering Geology*, *267*, 105478. https://doi.org/10.1016/j.enggeo.2020.105478

Milledge, D. G., Bellugi, D., McKean, J. A., Densmore, A. L., & Dietrich, W. E. (2014). A multidimensional stability model for predicting shallow landslide size and shape across landscapes. *Journal of Geophysical Research: Earth Surface*, *119*(11), 2481–2504. https://doi.org/10.1002/2014JF003135

Nereson, A. L., Davila Olivera, S., & Finnegan, N. J. (2018). Field and remote-sensing evidence for hydro-mechanical isolation of a long-lived earthflow in central California. *Geophysical Research Letters*, *45*(18), 9672–9680. https://doi.org/10.1029/2018GL079430

Nereson, A. L., & Finnegan, N. J. (2019). Drivers of earthflow motion revealed by an 80 yr record of displacement from Oak Ridge earthflow, Diablo Range, California, USA. *Geological Society of America Bulletin*, *131*(3–4), 389–402. https://doi.org/10.1130/B32020.1

Pathier, E., Fielding, E. J., Wright, T. J., Walker, R., Parsons, B. E., & Hensley, S. (2006). Displacement field and slip distribution of the 2005 Kashmir earthquake from SAR imagery. *Geophysical Research Letters*, *33*, L20310. https://doi.org/10.1029/2006GL027193

Roadifer, J. W., Forrest, M. P., & Lindquist, E. S. (2009). Evaluation of shear strength of mélange foundation at Calaveras Dam. *Proceedings of 29th U. S. Society for Dams, Annual Meeting and Conference: "Managing Our Water Retention Systems,"* pp. 507–521.

Roering, J. J. (2012). *Eel River, CA: Landsliding and the evolution of mountainous landscapes in collaboration with National Center for Airborne laser mapping (NCALM), distributed by Open Topography*. Retrieved from https://doi.org/10.5069/G9XS5S9P

Roering, J. J., Mackey, B. H., Handwerger, A. L., Booth, A. M., Schmidt, D. A., Bennett, G. L., & Cerovski-Darriau, C. (2015). Beyond the angle of repose: A review and synthesis of landslide processes in response to rapid uplift, Eel River, Northern California. *Geomorphology*, *236*, 109–131. https://doi.org/10.1016/j.geomorph.2015.02.013

Roering, J. J., Stimely, L. L., Mackey, B. H., & Schmidt, D. A. (2009). Using DInSAR, airborne LiDAR, and archival air photos to quantify landsliding and sediment transport. *Geophysical Research Letters*, *36*, L19402. https://doi.org/10.1029/2009GL040374

Rosen, P. A., Gurrola, E., Sacco, G. F., & Zebker, H. (2012). The InSAR scientific computing environment. *In 9th European Conference on Synthetic Aperture Radar, 2012, EUSAR*, pp. 730–733.

Rutter, E., & Green, S. (2011). Quantifying creep behaviour of clay-bearing rocks below the critical stress state for rapid failure: Mam Tor landslide, Derbyshire, England. *Journal of the Geological Society*, *168*(2), 359–372. https://doi.org/10.1144/0016-76492010-133

Schulz, W. H., Coe, J. A., Ricci, P. P., Smoczyk, G. M., Shurtleff, B. L., & Panosky, J. (2017). Landslide kinematics and their potential controls from hourly to decadal timescales: Insights from integrating ground-based InSAR measurements with structural maps and long-term monitoring data. *Geomorphology*, *285*, 121–136. https://doi.org/10.1016/j.geomorph.2017.02.011

Schulz, W. H., Smith, J. B., Wang, G., Jiang, Y., & Roering, J. J. (2018). Clayey landslide initiation and acceleration strongly modulated by soil swelling. *Geophysical Research Letters*, *45*(4), 1888–1896. https://doi.org/10.1002/2017GL076807

Simoni, A., Ponza, A., Picotti, V., Berti, M., & Dinelli, E. (2013). Earthflow sediment production and Holocene sediment record in a large Apennine catchment. *Geomorphology*, *188*, 42–53. https://doi.org/10.1016/j.geomorph.2012.12.006

Stumpf, A., Malet, J.-P., & Delacourt, C. (2017). Correlation of satellite image time-series for the detection and monitoring of slow-moving landslides. *Remote Sensing of Environment*, *189*, 40–55. https://doi.org/10.1016/j.rse.2016.11.007

Swanston, D. N., Ziemer, R. R., & Janda, R. J. (1995), Rate and mechanisms of progressive hillslope failure in the Redwood Creek basin, northwestern California. In K. M. Nolan, H. M. Kelsey, & D. C. Marron (Eds.) *Geomorphic processes and aquatic habitat in the Redwood Creek basin, Northwestern California. U.S. Geological Survey Professional Paper 1454*, (pp. E1–E16). Washington, DC: United States Government Printing Office.

Travelletti, J., & Malet, J.-P. (2012). Characterization of the 3D geometry of flow-like landslides: A methodology based on the integration of heterogeneous multi-source data. *Engineering Geology*, *128*, 30–48. https://doi.org/10.1016/j.enggeo.2011.05.003

Travelletti, J., Malet, J.-P., & Delacourt, C. (2014). Image-based correlation of laser scanning point cloud time series for landslide monitoring. *International Journal of Applied Earth Observation and Geoinformation*, *32*, 1–18. https://doi.org/10.1016/j.jag.2014.03.022

Van Asch, T. J., & Van Genuchten, P. M. B. (1990). A comparison between theoretical and measured creep profiles of landslides. *Geomorphology*, *3*(1), 45–55. https://doi.org/10.1016/0169-555X(90)90031-K

Van Asch, T. W., Van Beek, L., & Bogaard, T. (2007). Problems in predicting the mobility of slow-moving landslides. *Engineering Geology*, *91*(1), 46–55. https://doi.org/10.1016/j.enggeo.2006.12.012

Warrick, J. A., Ritchie, A. C., Schmidt, K. M., Reid, M. E., & Logan, J. (2019). Characterizing the catastrophic 2017 Mud Creek landslide, California, using repeat structure-from-motion (SfM) photogrammetry. *Landslides*, *16*, 1201–1219. https://doi.org/10.1007/s10346-019-01160-4

Wartman, J., Montgomery, D. R., Anderson, S. A., Keaton, J. R., Benoît, J., dela Chapelle, J., & Gilbert, R. (2016). The 22 March 2014 Oso landslide, Washington, USA. *Geomorphology*, *253*, 275–288. https://doi.org/10.1016/j.geomorph.2015.10.022

References From the Supporting Information

Aster, R. C., Borchers, B., & Thurber, C. H. (2013). Chapter Four - Tikhonov regularization. In R. C. Aster, B. Borchers, & C. H. Thurber (Eds.), *Parameter estimation and inverse problems (2nd ed.)* (pp. 93–127). Boston, MA: Academic Press. https://doi.org/10.1016/B978-0-12-385048-5.00004-5

Kasper, van W., John, A. S., William, N., & Luis, T. (2002). Data and model uncertainty estimation for linear inversion. *Geophysical Journal International*, *149*(3), 625–632. https://doi.org/10.1046/j.1365-246X.2002.01660.x